Journal of Magnetic Resonance 228 (2013) 116–124

Contents lists available at SciVerse ScienceDirect

Journal of Magnetic Resonance

journal homepage: www.elsevier.com/locate/jmr

EASY-GOING deconvolution: Automated MQMAS NMR spectrum analysis based on a model with analytical crystallite excitation efficiencies

Dennis L.A.G. Grimminck *, Bas van Meerten, Margriet H.W. Verkuijlen, Ernst R.H. van Eck, W. Leo Meerts, Arno P.M. Kentgens

Radboud University, Institute for Molecules and Materials, Heyendaalseweg 135, NL-6525 AJ Nijmegen, The Netherlands

ARTICLE INFO

Article history:
Received 1 November 2012
Revised 15 December 2012
Available online 4 January 2013

Keywords:
MQMAS fitting
Solid-state NMR
Evolutionary algorithms
Quadrupolar NMR
Czjzek distribution

ABSTRACT

The *EASY-GOING deconvolution* (*EGdeconv*) program is extended to enable fast and automated fitting of multiple quantum magic angle spinning (MQMAS) spectra guided by evolutionary algorithms. We implemented an analytical crystallite excitation model for spectrum simulation. Currently these efficiencies are limited to two-pulse and z-filtered 3QMAS spectra of spin 3/2 and 5/2 nuclei, whereas for higher spin-quantum numbers ideal excitation is assumed. The analytical expressions are explained in full to avoid ambiguity and facilitate others to use them. The *EGdeconv* program can fit interaction parameter distributions. It currently includes a Gaussian distribution for the chemical shift and an (extended) Czjzek distribution for the quadrupolar interaction. We provide three case studies to illustrate *EGdeconv*'s capabilities for fitting MQMAS spectra. The *EGdeconv* program is available *as is* on our website http://egdeconv.science.ru.nl for 64-bit Linux operating systems.

1. Introduction

Multi-dimensional NMR of quadrupolar nuclei is a powerful spectroscopic tool to provide spectral insights into nucleus-environment interactions at the molecular level [1]. A good example and immediate focus of this paper is the routinely used MQMAS experiment for half-integer quadrupolar nuclei [2,3]. This technique aids in distinguishing the contribution of the anisotropic part of the quadrupolar interaction from the isotropic chemical shift and quadrupolar induced shift in the F2 and F1 spectral dimensions. In practice this is especially useful for the analysis of one-dimensional spectra that have (strongly) overlapping lines.

Furthermore, NMR is a robust method for studying disordered materials, e.g., glasses and semiconductors, since it probes the local atomic environment of NMR active nuclei. This disorder is reflected in the MQMAS line shapes, and can be translated into interaction parameter distributions. In the last ten years there has been an increasing interest to quantify this disorder [4–6]. A model developed by Czjzek et al. [7] and extended by Le Caër et al. [5,6] is promising for describing the quadrupolar interaction parameter distribution resulting from this structural disorder. These models basically translate the distribution in electric field gradients, caused implicitly by variations in bond lengths and angles or disorder in the higher coordination spheres [8], to a distribution in interaction parameters.

In the NMR community the analysis of MQMAS spectra is currently facilitated by two programs; DMfit [1] for fitting with a simplified model, assuming ideal crystallite excitation, and SIMPSON [9] for accurate simulation incorporating all interactions. Regarding spectrum fitting, the computational costs for a single spectrum of the SIMPSON program are high. The main cause is the costly numerical integration of the Liouville-Von Neumann equation. The DMfit program is less broadly applicable, due to the assumption of ideal excitation of all crystallites, but allows spectrum fitting including a Czjzek distribution [4]. Another approach would be to use the GAMMA framework [10] that provides a versatile set of functionalities to simulate NMR experiments. It will require the user to program the NMR experiment and then connect it to a fitting routine. The presence of a Python interface (PyGAMMA) should make this procedure relatively easy.

This work aims to aid the quantitative analysis of MQMAS spectra [11] by the introduction of a fast fit-model that includes analytical crystallite excitation efficiencies. An approach that can be considered to partially fill the gap between SIMPSON and DMfit. The excitation efficiency model is available for 3QMAS spectra of spin 3/2 (^{7}Li, ^{23}Na, ^{39,41}K, ^{75}As, ^{87}Rb, ...) and 5/2 nuclei (^{17}O, ^{25}Mg, ^{27}Al, ^{85}Rb, ...). For higher spin quantum numbers an ideal excitation model is provided. Expressions were derived for a two-pulse and z-filtered MQMAS experiment in the infinitely fast MAS limit, thereby excluding simulation of spinning side bands. This approach enables a sub-second calculation of an MQMAS line shape, including a Gaussian chemical shift distribution, on a regular desktop computer, whereas a single-core SIMPSON simulation exceeds one hour.

* Corresponding author.
E-mail address: l.grimminck@science.ru.nl (D.L.A.G. Grimminck).

1090-7807/$ - see front matter © 2013 Published by Elsevier Inc.
http://dx.doi.org/10.1016/j.jmr.2012.12.012

Accounting for a distribution in quadrupolar parameters and multiple chemical sites is consequently relatively inexpensive. Furthermore, we provide parallel computation support and robust convergence of the fit by offering a choice between three evolutionary algorithms [12,13] to guide the fitting. A combination of MQMAS and one-dimensional NMR data can form a self-consistent data set for quantitative analysis, both supported by *EGdeconv* as is shown in the examples below.

The extension of EGdeconv [12] for MQMAS spectrum fitting has most functionalities of the one-dimensional fitting program, but excludes most importantly the library approach, thereby removing the second-party software dependence. In the remainder of this paper we will discuss the theory, the program structure and three case studies. Please note that this paper is not intended as a user manual for the program. A separate and up-to-date manual [14] is provided at our website http://egdeconv.science.ru.nl, where we also provide the input files for the examples.

2. Theory

The theory that follows is worked out specifically for spin 3/2 and 5/2 quadrupolar nuclei subjected to a two-pulse [2] or a z-filtered [3] 3QMAS scheme. Both experiments are illustrated in Fig. 1. The figures show how both experiments start with a radio frequency (rf) block-pulse to excite triple-quantum-coherence. Subsequently an incremented delay follows that forms the indirect dimension, after which a conversion pulse-scheme is used to obtain a detectable single quantum coherence to form the direct dimension. Finally the whole pulse scheme is phase cycled to exclusively obtain the required coherence pathway, all under MAS conditions.

Our aim is to present the analytical expressions in full for others to use without ambiguity. The manual [14] contains the expressions as they are actually implemented. We assume a static sample during the pulses and infinitely-fast MAS during the free evolution of the coherences. The implications of ignoring the time dependence of the crystallite orientations has been addressed in numerous papers [11,15–20]. It most of all concerns not simulating the redistribution of the spectral intensity in the spinning side bands in both dimensions. In our case studies we show how we can still obtain accurate and reliable interaction parameters and relative site abundances for this type of spectra. In the discussion section we will elaborate more on the range of validity of the model.

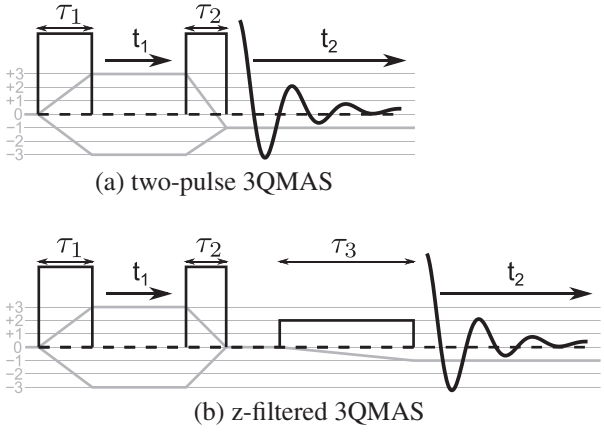

Fig. 1. Triple quantum magic angle spinning pulse sequences. The pulse sequences with their indirect t_1 and direct t_2 dimension are shown in black. Coherence pathways are shown in grey. (a) The two pulses of length τ_1 and τ_2 provide the triple-quantum-coherence excitation and conversion, respectively. (b) In the z-filtered 3QMAS experiment, the triple-quantum-coherence is excited and subsequently converted to zero-quantum-coherence. A third low-amplitude rf-pulse of width τ_3 provides a selective excitation of the detectable single-quantum-coherence.

In our approach, the MQMAS spectrum is described directly in the frequency domain. The contribution of every crystallite orientation to the spectrum is constructed by determining its frequency coordinate and the efficiency of the excitation before adding it to the powder average. We will refer to the model without excitation efficiency as ideal excitation model.

2.1. Crystallite spectral position

The spectrum of a crystallite in the infinitely-fast MAS case, is a single peak positioned at a two-dimensional frequency coordinate with components of the form [21]

$$\nu_{-m\to m} = 2m\nu_{iso} + C_0^{I,m}\nu_{qis} + C_4^{I,m}\nu_4(\alpha,\beta). \tag{1}$$

In the case of a 3QMAS experiment, the magnetic quantum numbers are $m = 1/2, 3/2$ for the direct and indirect dimension, respectively. I is the total nuclear angular momentum quantum number and the coefficients of the isotropic and anisotropic term of the quadrupolar interaction frequency are given by

$$C_0^{I,m} = 2m(I(I+1) - 3m^2), \tag{2}$$

$$C_4^{I,m} = 2m(18I(I+1) - 34m^2 - 5)\cdot P_4(\cos(\Theta_M)). \tag{3}$$

The fourth order Legendre polynomial term $P_4(\cos(\Theta_M))$, equal to $-7/18$ with Θ_M the magic angle, is a MAS averaged scaling factor. Furthermore ν_{iso}, ν_{qis} and $\nu_4(\alpha,\beta)$ in Eq. (1) are the isotropic chemical and quadrupolar induced shift and the anisotropic frequency contribution of the quadrupolar interaction. The latter two depend on the quadrupolar interaction parameters η (asymmetry) and C_q (quadrupolar coupling constant), two parameters we described in our previous EGdeconv paper [12], which are connected to Eq. (1) via

$$\nu_{qis} = -\frac{C_q^2(3+\eta)}{40\nu_0 I^2(2I-1)^2} \tag{4}$$

and

$$\nu_4(\alpha,\beta) = \frac{9C_q^2}{448\nu_0 I^2(2I-1)^2} \cdot\left\{\frac{7}{18}[3-\eta\cos(2\alpha)]^2\sin^4(\beta) + 2\left[\eta\cos(2\alpha) - 2 - \frac{\eta^2}{9}\right]\sin^2(\beta) + \frac{2}{45}\eta^2 + \frac{4}{5}\right\}. \tag{5}$$

Here $\nu_0 = -\gamma B_0/2\pi$ is the Larmor frequency of the quadrupolar nucleus, and α and β the Euler angles that connect the principal axes frame of the quadrupolar interaction to the MAS rotor frame, see Appendix A.

2.2. Crystallite excitation efficiency

We now proceed with the derivation of the crystallite excitation efficiencies. The approach consists of solving the time dependent Liouville-Von Neumann equation for the density operator involving both the multiple-quantum-coherence excitation pulse and the coherence-conversion pulse scheme. In addition to the assumptions of infinitely-fast MAS during free coherence-evolution and a static sample during pulsing, we neglect any rf-field offset [17,18]. An assumption that relies on the relatively strong quadrupolar interaction compared to practical rf-offsets, as will be addressed in the discussion section.

The relevant part of the density operator at thermal equilibrium in the rotating frame of the Zeeman interaction at time τ_0, is given by $\hat{\rho}(\tau_0) = \hat{I}_z$ and transforms after a block-pulse of length τ_1, see Fig. 1, according to

$$\hat{\rho}(\tau_1) = \exp\{-i\hat{H}\tau_1\}\hat{\rho}(\tau_0)\exp\{i\hat{H}\tau_1\}. \quad (6)$$

$\hat{H}$ is the Hamiltonian operator, in units of angular frequency, during an rf block-pulse. The Hamiltonian includes the rf-field and the first order quadrupolar interaction

$$\hat{H} = -\omega_1\hat{I}_x + \frac{\Omega_Q(\theta,\varphi)}{6}[3\hat{I}_z^2 - \hat{I}^2], \quad (7)$$

with $2\omega_1 = -\gamma B_{rf}$ and the quadrupolar frequency

$$\Omega_Q(\theta,\varphi) = \frac{\omega_Q}{2}[3\cos^2(\theta) - 1 + \eta\sin^2(\theta)\cos(2\varphi)]. \quad (8)$$

Here $\omega_Q = 6\pi C_q/[2I(2I-1)]$ and φ and θ are the Euler angles that connect the principal axes frame of the quadrupolar interaction to the laboratory frame, see Appendix A.

We now express the density operator in a basis of eigen functions $|I\ m\rangle$ of the Zeeman Hamiltonian, and calculate matrix element indices according to

$$\rho_{I+m'+1,I+m+1} \equiv \langle Im'|\hat{\rho}|Im\rangle. \quad (9)$$

To obtain the triple-quantum-coherence excited by the first pulse, we need to determine the triple-quantum-coherence matrix element at time τ_1. This requires the analytical diagonalisation of the Hamiltonian matrix given by Eq. (7) expressed in the appropriate Zeeman basis. Eq. (6) in the basis of eigen functions of the Hamiltonian directly returns the density matrix at time τ_1. After transformation back to the $|I\ m\rangle$ basis we obtain the triple-quantum-coherence term after the excitation pulse. Using Mathematica [22] we obtained for a spin 3/2 nucleus

$$\begin{aligned}\rho_{41}(\tau_1) = -\rho_{14}(\tau_1) = {} & \frac{3i\cos(\omega_1\tau_1)}{\omega_+^2 - \omega_-^2} \\ & \times [\{\Omega_Q\omega_- + \omega_1\omega_+\}\sin(\omega_+\tau_1) - \{\Omega_Q\omega_+ + \omega_1\omega_-\}\sin(\omega_-\tau_1)] \\ & + \frac{3i\sin(\omega_1\tau_1)}{2(\omega_+^2 - \omega_-^2)} \\ & \times \left[\left\{\omega_-^2 - \omega_+^2 - \Omega_Q^2\right\}\cos(\omega_+\tau_1) + \left\{\omega_-^2 - \omega_+^2 + \Omega_Q^2\right\}\cos(\omega_-\tau_1)\right]\end{aligned} \quad (10)$$

that clearly shows the involved sum and difference frequencies

$$2\omega_\pm = \sqrt{\Omega_Q^2 - 2\Omega_Q\omega_1 + 4\omega_1^2} \pm \sqrt{\Omega_Q^2 + 2\Omega_Q\omega_1 + 4\omega_1^2} \quad (11)$$

as well as the conventional pulse flip-angle $\omega_1\tau_1$.

We also obtained expressions for spin $I = 5/2$ where the Mathematica-based Hamiltonian diagonalisation of Man [23] was used. The symmetrical triple-quantum-coherence elements are

$$\rho_{52}(\tau_1) = -\rho_{25}(\tau_1) = \frac{i}{2}\sum_{m=1}^{3}\sum_{n=1}^{3}\frac{k_{mn}}{Q_{m+}Q_{n-}}\sin((\omega_{m+} - \omega_{n-})\tau_1). \quad (12)$$

The definitions of the variables are

$$Q_{m\pm} = \left[1 + \frac{5\omega_1^2}{4\left(\frac{10}{3}\Omega_Q - \omega_{m\pm}\right)^2} + \frac{2\omega_1^2}{\left(\frac{8}{3}\Omega_Q \pm \frac{3}{2}\omega_1 + \omega_{m\pm}\right)^2}\right] \quad (13)$$

and

$$k_{mn} = \left[3 + \frac{25\omega_1}{4\left(\frac{10}{3}\Omega_Q - \omega_{m+}\right)\left(\frac{10}{3}\Omega_Q - \omega_{n-}\right)} + \frac{2\omega_1}{\left(\frac{8}{3}\Omega_Q \pm \frac{3}{2}\omega_1 + \omega_{m+}\right)\left(\frac{8}{3}\Omega_Q \pm \frac{3}{2}\omega_1 + \omega_{n-}\right)}\right]. \quad (14)$$

The eigenvalues of the Hamiltonian matrix are

$$\begin{aligned}\omega_{1\pm} &= \mp\tfrac{\omega_1}{2} + 2\sqrt{\tfrac{s_\pm}{3}}\cos\left(\tfrac{\phi_\pm}{3}\right), \\ \omega_{2\pm} &= \mp\tfrac{\omega_1}{2} - 2\sqrt{\tfrac{s_\pm}{3}}\cos\left(\tfrac{\pi}{3} - \tfrac{\phi_\pm}{3}\right), \\ \omega_{3\pm} &= \mp\tfrac{\omega_1}{2} - 2\sqrt{\tfrac{s_\pm}{3}}\cos\left(\tfrac{\pi}{3} + \tfrac{\phi_\pm}{3}\right),\end{aligned} \quad (15)$$

with

$$\cos(\phi_\pm) = \frac{\Omega_Q}{18 s_\pm}\sqrt{\frac{3}{s_\pm}}\left(160\Omega_Q^2 \mp 36\Omega_Q\omega_1 - 144\omega_1^2\right) \quad (16)$$

and

$$s_\pm = \frac{84}{9}\Omega_Q^2 \pm 4\Omega_Q\omega_1 + 4\omega_1^2. \quad (17)$$

In the case of two-pulse 3QMAS data we are interested in the single-quantum-coherence created by the second pulse shown in Fig. 1a. By applying the approach for the first pulse to $\hat{\rho}(\tau_1)$ we obtained for spin $I = 3/2$

$$\begin{aligned}\rho_{23}(\tau_1 + \tau_2) = {} & \frac{3\omega_1^2}{2(\omega_+^2 - \omega_-^2)}[\rho_{14}(\tau_1) - \rho_{41}(\tau_1)] \times \cos(\omega_1\tau_2) \\ & \times \sin\left(\frac{1}{2}(\omega_+ + \omega_-)\tau_2\right)\sin\left(\frac{1}{2}(\omega_+ - \omega_-)\tau_2\right).\end{aligned} \quad (18)$$

The same procedure was applied for spin $I = 5/2$ resulting in the following expression

$$\begin{aligned}\rho_{34}(\tau_1 + \tau_2) = {} & \omega_1^2[\rho_{25}(\tau_1) - \rho_{52}(\tau_1)] \\ & \times \sum_{m=1}^{3}\sum_{n=1}^{3}\frac{\cos((\omega_{m+} - \omega_{n-})\tau_2)(Q_{m+}Q_{n-})^{-1}}{\left(\frac{8}{3}\Omega_Q + \frac{3}{2}\omega_1 + \omega_{m+}\right)\left(\frac{8}{3}\Omega_Q - \frac{3}{2}\omega_1 + \omega_{n-}\right)}.\end{aligned} \quad (19)$$

In the case of z-filtered 3QMAS experiments, see Fig. 1b, we consider the efficiency directly proportional to the population difference of the central-transition states. For a spin $I = 3/2$ this is

$$\rho_{22}(\tau_1 + \tau_2) - \rho_{33}(\tau_1 + \tau_2) = -2i\tan(\omega_1\tau_2)\rho_{23}(\tau_1 + \tau_2). \quad (20)$$

This assumes ideal conversion of the zero-quantum coherence to single-quantum coherence during the selective third pulse of length τ_3 in the experiment, feasible by choosing the appropriate rf-field [24,25]. For spin $I = 5/2$ the expression for $\rho_{33}(\tau_1 + \tau_2) - \rho_{44}(\tau_1 + \tau_2)$ is equal to the right hand side of Eq. (19) multiplied by -2i and the cosine function replaced with a sine [14].

2.3. Ideal crystallite excitation

In this work we define ideal crystallite excitation as the spectral line shape is directly determined by the number of crystallite orientations that are mapped to each two-dimensional frequency coordinate with components given by Eq. (1). In other words, the excitation efficiency has a negligible angular dependence. In general this situation is created by using short pulses; no differentiation in coherence-evolution of the crystallites during the pulse. And additionally sufficient field strength to fully cover the spectral width of the line shape; a negligible rf-offset dependence.

3. The program

As noted above, the model for MQMAS spectrum simulation is build into the *EGdeconv* program [12], a framework that provides parallelised evolutionary algorithms to guide the data fitting. Therefore we will only describe the MQMAS simulation model here, and refer to the previous paper [12] and the accompanying

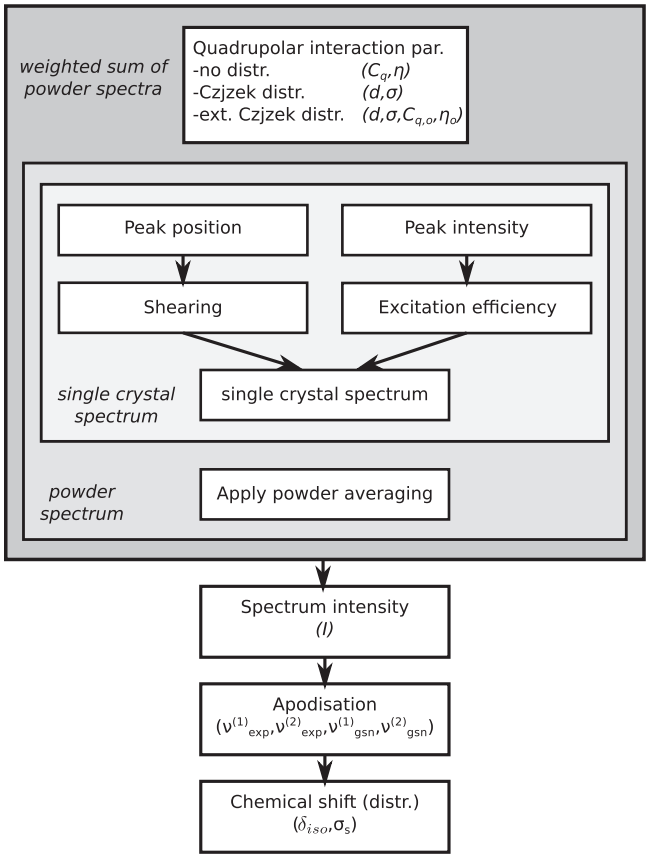

Fig. 2. The scheme used by *EGdeconv* to compute a subspectrum corresponding to a chemical site. Depending on if the quadrupolar interaction parameters have a distribution, crystallite spectra are summed per C_q, η pair to form a powder spectrum and subsequently summed according to a distribution over C_q, η pairs. Furthermore, the subspectrum receives a relative intensity, line broadening and a convolution with a Gaussian distribution for the chemical shift. Parameters that are indicated in the figure are available in each parameter set in the input file.

manual [14] for further information on the parameters and keywords used in the input file of the *EGdeconv* program.

We now proceed with the description of the synthesis of a subspectrum. A subspectrum corresponds to a chemical site and the sum of subspectra is the simulated spectrum that is used to fit the experimental data. Fig. 2 shows the different steps of the calculation. All variables presented in the figure are directly controlled via a parameter set in the *EGdeconv* input file. The heart of the simulation in Fig. 2 is the crystallite spectrum. It is created by combining the frequency coordinate components given by Eq. (1) and the corresponding, but optional, excitation efficiency Eqs. (18), (19) or (20). The program allows to apply a shearing transformation [21] as a function of λ according to

$$\nu^{sheared}_{-m\to m} = \nu_{-m\to m} - \lambda\nu_{-1/2\to 1/2}. \tag{21}$$

A crystallite spectrum is generated per C_q, η pair and subsequently summed over all orientations in a powder average. Currently only the ZCW (Zaremba, Conroy, Wolfsberg) averaging scheme [26] is implemented. Two-angle sets are used, with an equidistant integration over the third angle described in appendix Appendix A and [14]. The quadrupolar interaction parameters may be distributed, currently supported by the (extended) Czjzek distribution, which involves a weighted sum over the generated powder spectra.

After all summations are done, the subspectrum is multiplied with an overall intensity factor that corresponds to the relative abundance of a chemical site in the material. Additionally the two-dimensional line shape can be broadened with a Gaussian and/or exponential apodisation to, e.g., match the data processing or include the dephasing effects of dipolar couplings. The final step is the convolution of the spectrum with an optional (Gaussian) chemical shift distribution. This distribution has a mean δ_{iso} and a width σ_s [14].

4. Examples

In this section we present the results of several case studies each of which represents a different part of the program's capabilities. We start by benchmarking *EGdeconv* by fitting several ^{27}Al 3QMAS spectra, nuclear spin 5/2, of aluminium alkoxides. Quadrupolar interaction parameters of the alkoxides were determined by [27] by fitting one-dimensional data. Their 3QMAS data was used to determine the isotropic chemical shifts. In this case study we show how we obtain all these parameter values directly from the 3QMAS spectra and how spinning side bands are handled.

Subsequently we present the fit of ^{87}Rb 3QMAS data, nuclear spin 3/2, of rubidium-nitrate measured under experimental conditions that lead to non-ideal excitation, thereby putting our fitting model with analytical excitation efficiencies to the test. In addition to reproducing the interaction parameters of [28], we prove that we can reproduce the line shape and relative site intensities where the ideal excitation model does not.

To conclude we show the analysis of the 3QMAS spectrum of an yttrium-sialon glass. This spectrum reflects a distribution in both quadrupolar interaction parameters and chemical shift, that we try to model with respectively a Czjzek and Gaussian distribution and the analytical excitation efficiencies. We show how we can fit the line shapes of three sites simultaneously to obtain their interaction distribution parameters. The interaction parameters can subsequently be used to deconvolute the one-dimensional spectrum, and obtain the relative site abundances.

All fits include the excitation efficiencies, unless stated otherwise, and were performed with the Covariance matrix adaptation evolution strategies (CMA-ES) algorithm [29]. The *EGdeconv* input files of all MQMAS examples are available on our website http://egdeconv.science.ru.nl.

4.1. Aluminium alkoxides

In Fig. 3 the ^{27}Al sheared 3QMAS data fits of three different alkoxides coordinated to aluminium are presented. All spectra were measured and analysed in ref. [27] on the basis of one-dimensional and 3QMAS data. Table 1 summarises our resulting parameter values from the 3QMAS fit, alongside their values from the previous study [27]. In all spectra the sum-projections in both direct and indirect dimensions of the two-dimensional experimental and simulated data are shown. A least-squares [14] between these projections was used as a measure of fit-quality for the CMA-ES algorithm. The obvious benefit of the sum-projections is that the intensity of the spinning side bands is added to that of the central transition in the δ_2 dimension, which can be more readily simulated. The δ_1 dimension sum-projection provides in these spectra an extra feature to determine the isotropic position of the central transition during the fitting.

The spectrum of aluminium ethoxide, Fig. 3a, that corresponds to a five-coordinated aluminium, shows a good match between the sum-projections in the (δ_2) dimension. The main difference at high δ_2 values in the figure is caused by an Al_2O_3 impurity. For the case of aluminium butoxide, Fig. 3b, with a tetrahedral aluminium surroundings the fitted spectrum also closely resembles the sum-projection of the experimental data. The line shape at $\delta_1 \approx 250$ ppm is an aliased spinning side band. Table 1 shows that we obtained

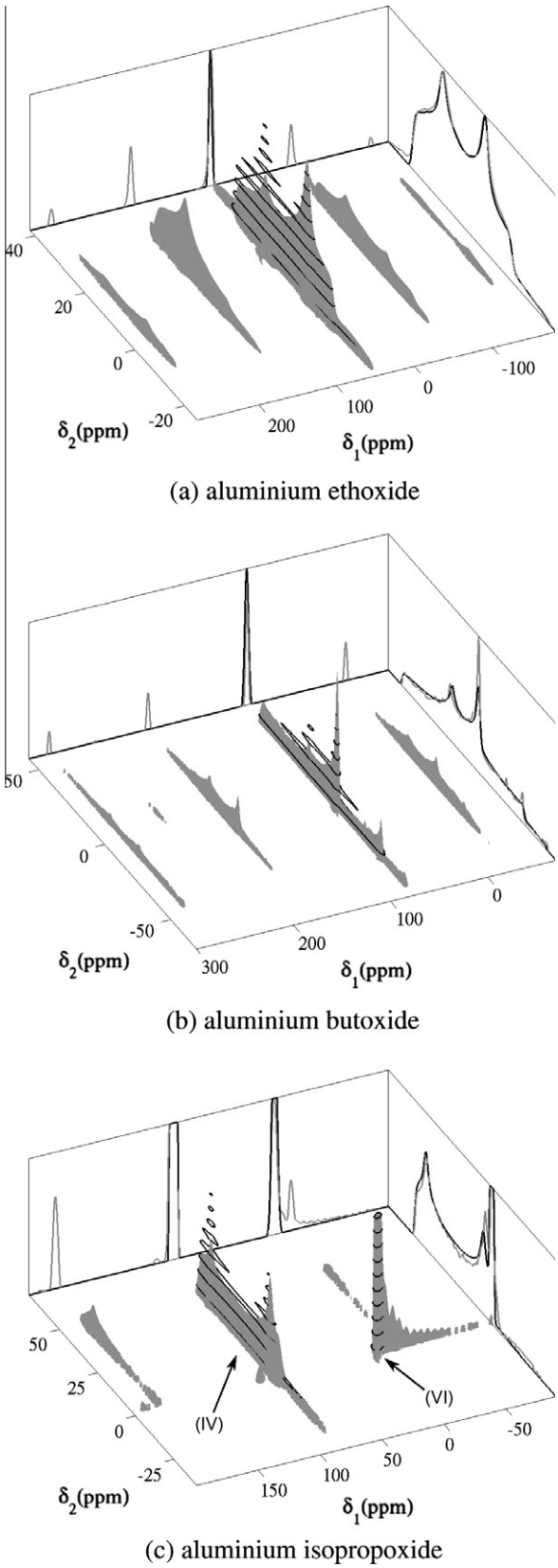

Fig. 3. ^{27}Al z-filtered 3QMAS spectra ($\omega_1/2\pi$ = 310 kHz, τ_1 = 1.3 μs, τ_2 = 0.45 μs, and τ_3 = 4 μs with $\omega_1/2\pi$ = 21 kHz), experiment (grey) and fit (black), for three aluminium alkoxides [27]. The spectra are normalised based on their integrals, and their sum-projections are scaled with their integrals to be visible on the intensity scale of the spectrum. The isopropoxide spectrum is zoomed in on its tetrahedral (IV) site, this is the reason for the cut of the octahedral (VI) site peak. Data was sheared after the fit.

Table 1
Fitted interaction parameters for the alkoxide spectra in Fig. 3, values from [27] are in italics. In the fit of isopropoxide, η of the octahedral site was fixed at 0.

	δ_{iso} (ppm)		C_q (MHz)		η	
Ethoxide	35.5	*35.5*	9.58	*9.65*	0.37	*0.39*
Butoxide	48.5	*48.5*	13.03	*13.14*	0.64	*0.61*
Isoprop. (IV)	60.0	*61.5*	12.20	*12.37*	0.14	*0.14*
(VI)	0.8	*2.5*	0.6	*1.9*	0.0	*0.0*

Table 2
Fitted parameter values of the ^{87}Rb 3QMAS spectra of rubidium-nitrate in Fig. 4. *I*, as indicated in Fig. 2, stands for relative intensity, in this case with respect to site I. For comparison the parameter values obtained by [30] at 29.3 °C are given in the most-right column.

Site	Pars	(Fig. 4a) ideal	(b) Eff. off	(c) Eff. on	[30]
I	C_q (MHz)	1.75	1.77	1.74	1.77
	η	0.54	0.60	0.55	0.54
II	C_q (MHz)	1.72	1.75	1.73	1.72
	η	0.19	0.27	0.16	0.19
	I	0.97	0.90	1.06	1.00
	Integral	1.14	0.93	0.93	–
III	C_q (MHz)	1.99	1.99	1.99	2.01
	η	0.89	0.93	0.91	0.90
	I	1.00	0.85	0.99	1.00
	Integral	0.93	0.87	0.87	–

interaction parameters that agree with the findings of [27] on the basis of MQMAS and one-dimensional data for both spectra.

The spectrum of aluminium isopropoxide in Fig. 3c reveals a tetrahedral (IV) and octahedral (VI) site that posed the opportunity to determine relative site abundances. From the fit of these relative intensities we obtained the ratio (IV):(VI) = 1:2.7 which was determined 1:3 by [27] on the basis of one-dimensional data. It should be noted that there is a negligible difference between the fitted relative intensities, whether the analytical excitation efficiencies are accounted for or not. This means that with the current pulse widths both sites are excited with similar efficiency. The difference for C_q of the octahedral site (VI) is due to a lack of quadrupolar features in the sharp line.

4.2. Rubidium-nitrate

Rubidium-nitrate ($RbNO_3$), as the guinea pig for MQMAS experiments, has three well-defined sites with: equal abundance, similar quadrupolar coupling constants, but different asymmetry parameters as given in the most-right column in Table 2.

To further test the analytical excitation efficiency model and distinguish it from the ideal excitation model, two ^{87}Rb 3QMAS spectra of $RbNO_3$ were measured. One spectrum was obtained using relatively short pulses and strong rf-field strength and represents the ideal excitation case (Fig. 4a), as discussed in Section 2.3. The second spectrum was obtain with complementary settings to evoke non-ideal excitation (Fig. 4b and c). By measuring the spectrum at a magnetic field of 300 MHz proton frequency we also encountered overlapping lines as an additional challenge for the fitting.

A fit of the ideal excitation spectrum using either model results in Fig. 4a. The least squares difference between the two-dimensional experimental and simulated spectra was used [14] as the quality measure for the CMA-ES algorithm. Table 2 shows that the fitted parameter values are nearly equal to those from literature [30]. This is a confirmation that the assumption of ideal excitation is valid in this case.

Fitting the second spectrum resulted in a different fit for each model as shown in Fig 4b and c. Incorporation of the (analytical)

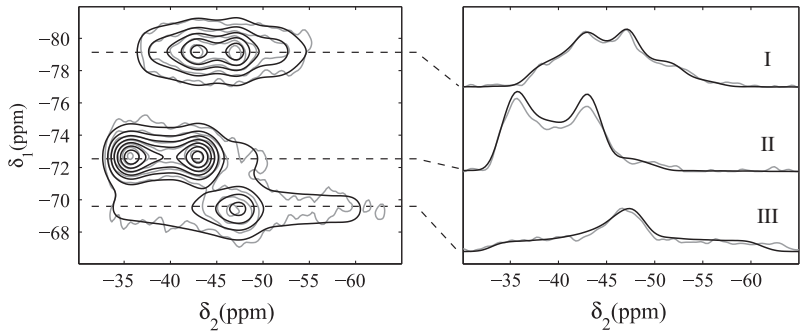

(a) excitation efficiency model fit to ideal excitation data

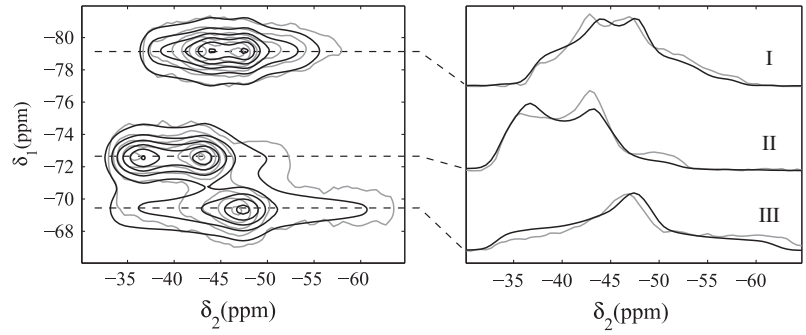

(b) ideal excitation model fit to non-ideal excitation data

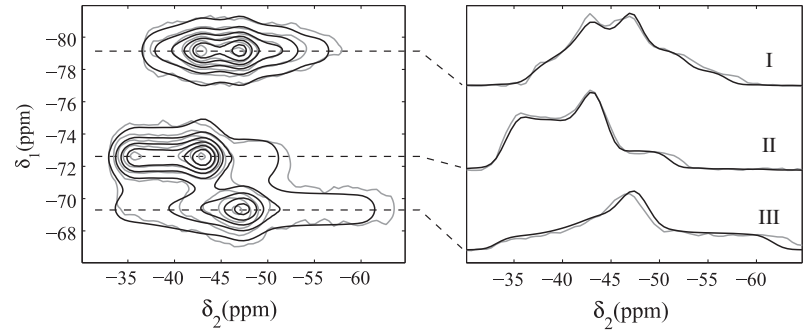

(c) excitation efficiency model fit to non-ideal excitation data

Fig. 4. Simulations (black) of the z-filtered ^{87}Rb 3QMAS spectrum of rubidium-nitrate (grey). Integrals of the spectra are set equal, contour lines are drawn at the same intensities. (a) ideal excitation spectrum ($\omega_1/2\pi$ = 211 kHz, τ_1 = 2.6 μs, τ_2 = 0.9 μs) fitted with excitation efficiency model. (b) and (c) the non-ideal excitation spectrum ($\omega_1/2\pi$ = 108 kHz, τ_1 = 5.2 μs, τ_2 = 2.6 μs) fitted with and without analytical excitation efficiencies.

excitation efficiencies provides a better description of especially line shapes I and II. This is reflected in a difference in η parameter for both fits as shown in Table 2. Particularly line shape II is different from that in Fig. 4a. The intensity of the left peak appears to move into the right shoulder of the line.

With respect to the prediction of relative site abundances, it follows from Table 2 that the excitation model fit comes closest to the actual ratio. Especially if we compare the sum of the intensities (due to the overlap of the line shapes), we obtain the ratios 1:2.05 and 1:1.75. The ideal excitation model appears to follow the trend of the line shape integrals, which leads to an underestimation of the intensities of lines II and III.

4.3. Yttrium-sialon glass

Sialon glasses doped with rare-earth metals are interesting for photo-electric applications. Glasses are disordered systems which makes quantification in terms of interaction constants tedious. The benefit of having MQMAS data is that it aids in effectively separating chemical shift and quadrupolar interaction contributions to the spectrum, that would otherwise not be visible in the one-dimensional data.

In practice this means that, after shearing, a distribution in chemical shift will become visible as a broadened line in the F1 dimension. For a distribution in quadrupolar interaction parameters, the line shape is influenced in both dimensions by the (isotropic) quadrupolar induced shift, however, only the F2 dimension is influenced by the anisotropic part of the interaction. The two-dimensional spectrum thereby provides enough features to distinguish and fit interaction parameter distributions, and potentially relative site abundances as discussed in the rubidium-nitrate case study.

Fig. 5a shows the fitted ^{27}Al 3QMAS spectrum of an yttrium-sialon glass [31] (named after the atomic constituents: silicium, aluminium, oxygen and nitrogen), using the inner product cost function [14] between the two-dimensional spectra as the quality measure. In both dimensions of the spectrum we see broadened lines which indicates both chemical shift and quadrupolar interactions are distributed. In the two-dimensional plane, the lines are

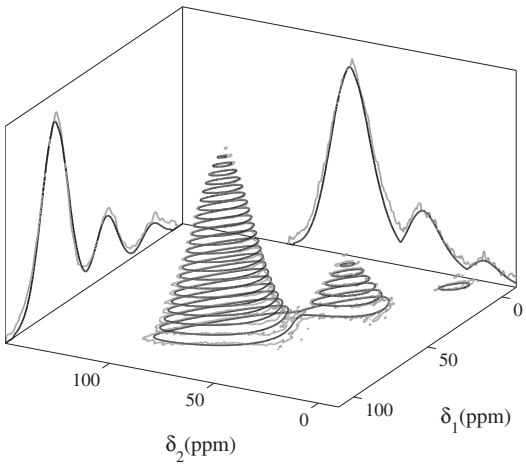

(a) yttrium-sialon glass 3QMAS

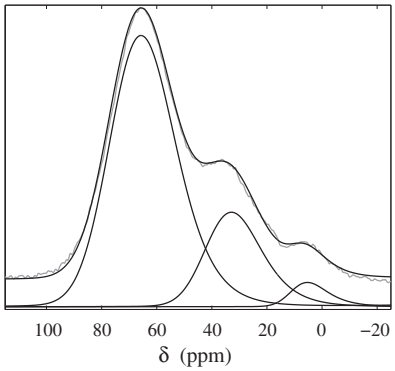

(b) yttrium-sialong lass one-pulses pectrum

Fig. 5. Experimental data is in shown in grey, simulated results are in black. (a) Fitted ^{27}Al 3QMAS spectrum of an yttrium-sialon glass with skyline projections. Three chemically distinct sites are shown that correspond to variations in, from bottom to top: tetrahedral, trigonal bipyramidal and octahedral surroundings. A Czjzek and Gaussian distribution is used for the quadrupolar interaction and chemical shift, respectively. Fitted parameter values are given in Table 3. (b) Fit of the one-pulse spectrum. Czjzek distribution parameter values from the 3QMAS fit are used (Table 3). The subspectra that constitute the simulated spectrum are plotted below the base line.

separated which is useful to avoid ambiguity in the fit. Note the one-pulse spectrum of the sialon material in Fig. 5b does not provide these insights.

The three distinct lines of the chemical sites in the spectrum are probably broadened due to structural variations in bond angles and lengths deviating from: tetrahedral, trigonal bipyramidal and octahedral coordinations in the material [32]. Fig. 5a shows how a combination of the Czjzek distribution for the quadrupolar interaction parameters and a Gaussian distribution for the chemical shift can approximate the line shapes in the spectrum. Only at the basis of the largest peak a mismatch is visible between the more triangular basis of the experimental data and the more rounded simulated spectrum. Table 3 presents the fitted parameter values. It should be noted that a fit with either ideal or excitation efficiency model did not change the results. Together with the fact that the intensities match with the line integrals, we may conclude ideal excitation of the material.

The fitted interaction parameters of the 3QMAS were used to fit the one-pulse spectrum of the yttrium-sialon glass. This led to a good and stable fit as shown in Fig. 5b. Note that the asymmetric line shape of the subspectra is caused by the Czjzek distribution. Table 3 shows the fitted relative intensities of the lines. There is

Table 3
The parameter values from the fit of the yttrium-sialon glass (Fig. 5). Parameters δ_{iso}, σ_s are the mean and width of the Gaussian chemical shift distribution, σ the width of the Czjzek distribution (power factor $d = 5$), 2D integrals of the lines in Fig. 5a, I the relative intensities of Fig. 5a and b.

Coordination	δ_{iso} (ppm)	σ_s (ppm)	σ (MHz)	2D integral	2D I	1D I
Tetrahedral	62.6	17.0	4.03	1.00	1.00	1.00
Trigon. bip.	27.7	13.6	4.04	0.21	0.20	0.30
Octahedral	−2.4	11.4	3.65	0.03	0.04	0.05

a significant difference for the MQMAS and 1D fit with respect to the tetrahedral and trigonal bipyramidal site intensity ratios. This difference we explain by the different effective T1 > 2 s of the two sites in combination with the cycle delay of 4 s that was used to limit the time needed for the 3QMAS experiment. The one-pulse data should be quantitative since only a short pulse, and therefore a small flip-angle, is used.

5. Discussion

A large part of this paper is focussed on the analytical excitation efficiencies to extend the accuracy of fast MQMAS spectrum simulation. Here we would like to elaborate on the limits of the validity of the theory by using physical arguments and tests we performed.

One of the first assumptions is that the spin system can be treated as static during the pulsing. An important argument in favour of this, is the order of magnitude difference between the pulse widths of several μs (equivalent to hundreds of kHz) and the MAS speeds of several tens of kHz. In addition to the argument of a small γ angle rotation Appendix (A) of the MAS rotor, typically of the order of 10 degrees, the positions of the crystallites along the direction of rotation are interchanged. This leads to a further indistinction for the crystallite excitation efficiency. If the pulse becomes too long or the MAS speed too high, the excitation efficiency will be influenced, and our model will no longer be valid. Pulse lengths can be shortened by increasing the rf-field strength [21]. Whether or not the use of our model is valid should be assessed per experiment. For the case study of the sialon glass, at 37 kHz MAS, the line shapes could be reproduced accurately.

For testing purposes we used SIMPSON as well as our own numerical integration routine to solve the Liouville-Von Neumann equation including the full quadrupolar interaction Hamiltonian, rf-field and sample rotation for a single crystallite. Although we did not thoroughly study all of the parameter dependencies, for typical pulse widths and interaction parameters, related to the examples, our perturbative method did not significantly deviate from the exact solution. SIMPSON additionally accounts for MAS and second order quadrupolar coupling. The results started to deviate for MAS speeds above 30 kHz and pulse widths larger than 10 μs. This shows our model is realistic for a wide range of experimental settings.

Secondly we assume an ideal zero to single quantum conversion pulse in a z-filtered 3QMAS experiment. Which should be acceptable with a properly chosen rf-field for the z-filter pulse [24,25]. We experimentally verified the correctness of the assumption by comparing two-pulse data with z-filtered data at different rf-field strengths for the rubidium-nitrate. Additionally our testing program showed the explicit incorporation of the third pulse does not alter the results for typical experimental settings.

Thirdly we disregard rf-offset, which is acceptable given the tilt angle of the nutation does not deviate much for line widths of several kHz and rf-field strengths of hundred kHz or more. If necessary, it is possible to implement analytical excitation efficiencies including rf-offset [17,18].

The assumption that proves the more difficult to handle is the infinitely-fast spinning limit. Spinning side bands are often visible

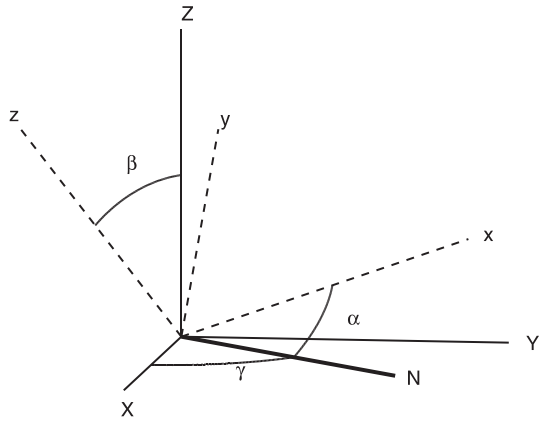

Fig. A.6. Definition of the Euler angles (α, β, γ) that relate the interaction's principal axes frame (x, y, z) to the reference frame (X, Y, Z). Note that the vector N is normal to the plane of the z and Z axes.

in the spectrum, so this immediately proves this assumption is incorrect. In order to still obtain reliable results it is important to have all spinning side bands present in the spectrum, so all spectral intensity can be regained in the sum-projections so the projections can be fitted as shown in the alkoxides example. A practical solution may be to perform rotor synchronised detection experiments [33], in order for all side bands to fold back on top of the central peak.

To conclude, in addition to obtaining the correct line shape and thereby the quadrupolar interaction parameters, it is also feasible to obtain the relative abundance of the sites directly from the MQMAS data, as was shown in the rubidium-nitrate example. In the yttrium-sialon case study, however, we encountered a problem due to the requirement of a relatively long cycle delay in the experiment due to the different effective T1's of the sites. In such cases it is easier to obtain the interaction parameter information from the MQMAS data and use these to fit a one-pulse spectrum to obtain quantitative relative intensities.

6. Conclusions

We have shown the capabilities of the *EGdeconv* program to fit, guided by evolutionary algorithms, MQMAS spectra using an analytical crystallite excitation efficiency model. We presented the theory for the model in full detail to avoid ambiguity and to facilitate others to use it. In three case studies we showed how to obtain quantitative information from fitting 3QMAS spectra with: spinning side bands, multiple sites, interaction parameter distributions and non-ideal excitation. The ideal excitation model encompasses all quadrupolar nuclei and multiple-quantum-coherence excitation, while excitation efficiencies are available for I = 3/2, 5/2 nuclei and two-pulse and z-filtered 3QMAS.

7. Experimental

7.1. 1D sialon fit

For the fit of the 1D spectrum of the yttrium-sialon glass with the *EGdeconv* program, a library size of 609 files, simulated with SIMPSON, was used with C_q ranging from 1 to 15 MHz in steps of 0.5 MHz and η from 0 to 1 in steps of 0.05.

7.2. Yttrium-sialon

The single-pulse and MQMAS experiments were performed on an 850 MHz Varian spectrometer at a MAS frequency of 37 kHz, with AlCl(aqua) as reference compound for ^{27}Al at 221 MHz.

A pulse length of 1.4 μs and a rf-field strength of 20 kHz was used in the single-pulse experiment. The z-filtered 3QMAS experiment was performed with an rf-field strength of 150 kHz for the excitation and conversion pulses with a pulse length of 2.4 and 0.8 μs respectively. The z-filter pulse was 5 μs long at an rf-field of 20 kHz.

Both single-pulse and MQMAS spectrum were corrected for aluminium background of the rotor. The rotor signal was measured with the same experimental settings and subsequently subtracted from the spectra.

7.3. Rubidium-nitrate

The ^{87}Rb z-filtered 3QMAS spectrum was measured on a 300 MHz Varian spectrometer at 12.5 kHz MAS. The non-ideal excitation data was obtained using an rf-field strength of 105 kHz for the excitation and conversion pulses with lengths 5.2 and 1.8 μs, respectively. For the ideal excitation data the rf-field settings were: 211 kHz field strength and pulse widths of 2.6 and 0.9 μs. The z-filter pulse had a strength of 10 kHz and width of 11 μs. A reference of RbCl(aqua) was used for ^{87}Rb at 96 MHz.

Acknowledgments

D.G. thanks Wim J. van der Zande for suggestions during the preparation of this paper's manuscript. The authors thank Dr. Bert H.T.J.M. Hintzen (TU/e) for providing the yttrium-sialon material.

Appendix A. Frame interconversion

Eqs. (1) and (7) for the position and intensity of a single crystal spectrum are defined with respect to the MAS and laboratory reference frame, respectively. Fig. A.6 illustrates how the Euler angles relate the principal axes frame (x,y,z) of the quadrupolar interaction tensor to a reference frame, either the MAS frame (Z along the MAS axis) with α, β, γ or laboratory frame (Z along the magnetic field) where we use φ, θ, ψ in this work.

It is the infinitely-fast MAS assumption and cylindrical symmetry of the magnetic field that render Eqs. (1) and (7) invariant to the γ and ψ angle. When we, however, want to relate a frequency coordinate to an excitation efficiency we need to relate the angles to each other. We worked out the following relations

$$\begin{aligned}\cos(\theta) &= -\sin(\Theta_M)\sin(\beta)\cos(\gamma)+\cos(\Theta_M)\cos(\beta),\\ \cos(\varphi) &= \sin(\Theta_M)[\cos(\alpha)\cos(\beta)\cos(\gamma)-\sin(\alpha)\sin(\gamma)]\\ &\quad +\cos(\Theta_M)\cos(\alpha)\sin(\beta),\end{aligned} \tag{A.1}$$

from which we can construct all terms in Eq. (8) using goniometric identities.

Appendix B. Supplementary material

Supplementary data associated with this article can be found, in the online version, at http://dx.doi.org/10.1016/j.jmr.2012.12.012.

References

[1] D. Massiot, F. Fayon, M. Capron, I. King, S. Le Calvé, B. Alonso, J. Durand, B. Bujoli, Z. Gan, G. Hoatson, Modelling one- and two-dimensional solid-state NMR spectra, Magn. Reson. Chem. 40 (2002) 70–76.
[2] L. Frydman, J.S. Harwood, Isotropic spectra of half-integer quadrupolar spins from bidimensional magic-angle spinning NMR, J. Am. Chem. Soc. 117 (1995) 5367–5368.
[3] J. Amoureux, C. Fernandez, S. Steuernagel, Z filtering in MQMAS NMR, J. Magn. Reson. Ser. A 123 (1996) 116–118.
[4] J. d'Espinose de Lacaillerie, C. Fretigny, D. Massiot, MAS NMR spectra of quadrupolar nuclei in disordered solids: the Czjzek model, J. Magn. Reson. 192 (2008) 244–251.

[5] G. Le Caër, R.A. Brand, General models for the distributions of electric field gradients in disordered solids, J. Phys.: Condens. Matter 10 (1998) 10715–10774.
[6] G. Le Caër, B. Bureau, D. Massiot, An extension of the czjzek model for the distributions of electric field gradients in disordered solids and an application to NMR spectra of ^{71}Ga in chalcogenide glasses, J. Phys.: Condens. Matter 22 (2010) 065402.
[7] G. Czjzek, J. Fink, F. Götz, H. Schmidt, J.M.D. Coey, J.P. Rebouillat, A. Liénard, Atomic coordination and the distribution of electric field gradients in amorphous solids, Phys. Rev. B 23 (1981) 2513–2530.
[8] P.J. Knijn, P.J.M. van Bentum, E.R.H. van Eck, C. Fang, D.L.A.G. Grimminck, R.A. de Groot, R.W.A. Havenith, M. Marsman, W.L. Meerts, G.A. de Wijs, A.P.M. Kentgens, A solid-state NMR and DFT study of compositional modulations in Al_xGa_{1-x} As, Phys. Chem. Chem. Phys. 12 (2010) 11517–11535.
[9] M. Bak, J. Rasmussen, N. Nielsen, SIMPSON: a general simulation program for solid-state NMR spectroscopy, J. Magn. Reson. 147 (2000) 296–330.
[10] S.A. Smith, T.O. Levante, B.H. Meier, R. Ernst, Computer simulations in magnetic resonance. an object-oriented programming approach, J. Magn. Reson. Ser. A 106 (1994) 75–105.
[11] S. Ding, C.A. McDowell, Quantification of mqmas spectra of solids containing quadrupolar nuclei, Chem. Phys. Lett. 307 (1999) 215–219.
[12] D.L.A.G. Grimminck, B.J.W. Polman, A.P.M. Kentgens, W.L. Meerts, EASY-GOING deconvolution: combining accurate simulation and evolutionary algorithms for fast deconvolution of solid-state quadrupolar NMR spectra, J. Magn. Reson. 211 (2011) 114–120.
[13] M. Wächtler, A. Schweitzer, T. Gutmann, H. Breitzke, G. Buntkowsky, Efficient analysis of ^{51}V solid-state MAS NMR spectra using genetic algorithms, Solid State Nucl. Magn. Reson. 35 (2009) 37–48.
[14] D.L.A.G. Grimminck, B. van Meerten, W.L. Meerts, Description and features of the program egdeconv: automated assign and fit programs for powder nmr spectra using evolutionary algorithms, EGdeconv manual, 2012. <http://egdeconv.science.ru.nl>.
[15] L. Marinelli, L. Frydman, On the origin of spinning sidebands in MQMAS NMR experiments, Chem. Phys. Lett. 275 (1997) 188–198.
[16] S.Z. Ageev, B.C. Sanctuary, Analytical solutions for spin 7/2 line-intensities in solid-state NMR, Mol. Phys. 84 (1995) 835–844.
[17] S. Ageev, B. Sanctuary, Analytical solutions for spin 3/2 off-resonance line intensities in solid state NMR, Chem. Phys. Lett. 255 (1996) 71–78.
[18] A. Kentgens, Off-resonance nutation nuclear magnetic resonance spectroscopy of half-integer quadrupolar nuclei, Prog. Nucl. Mag. Res. Sp. 32 (1998) 141–164.
[19] G.M. Muha, Exact solution of the eigenvalue problem for a spin 3/2 system in the presence of a magnetic field, J. Magn. Reson. 53 (1983) 85–102.
[20] R.B. Creel, Analytic solution of fourth degree secular equations: $I = 3/2$ Zeeman-quadrupole interactions and $I = 7/2$ pure quadrupole interaction, J. Magn. Reson. 52 (1983) 515–517.
[21] A.P.M. Kentgens, A practical guide to solid-state NMR of half-integer quadrupolar nuclei with some applications to disordered systems, Geoderma 80 (1997) 271–306.
[22] Wolfram Research, Inc., Mathematica Edition: Version 8.0, 2010.
[23] P.P. Man, Analytical expression for the spin-5/2 line intensities, Mol. Phys. 78 (1993) 307–318.
[24] N.M. Trease, K.K. Dey, P.J. Grandinetti, Optimum excitation of enhanced central transition populations, J. Magn. Reson. 200 (2009) 334–339.
[25] T.T. Nakashima, K.J. Harris, R.E. Wasylishen, Pulse FT NMR of non-equilibrium states of half-integer spin quadrupolar nuclei in single crystals, J. Magn. Reson. 202 (2010) 162–172.
[26] V.B. Cheng, J. Henry, H. Suzukawa, M. Wolfsberg, Investigations of a nonrandom numerical method for multidimensional integration, J. Chem. Phys. 59 (1973) 3992–3999.
[27] A. Abraham, R. Prins, J.A. van Bokhoven, E.R.H. van Eck, A.P.M. Kentgens, Multinuclear solid-state high-resolution and ^{13}C–^{27}Al double-resonance magic-angle spinning NMR studies on aluminum alkoxides, J. Phys. Chem. B 110 (2006) 6553–6560. PMID: 16570954.
[28] R. Siegel, T.T. Nakashima, R.E. Wasylishen, Sensitivity enhancement of MQMAS NMR spectra of spin 3/2 nuclei using hyperbolic secant pulses, Chem. Phys. Lett. 403 (2005) 353–358.
[29] N. Hansen, A. Ostermeier, Completely derandomized self-adaptation in evolution strategies, Evol. Comput. 9 (2001) 159–195.
[30] J. Skibsted, H.J. Jakobsen, Variable-temperature ^{87}Rb magic-angle spinning NMR spectroscopy of inorganic rubidium salts, J. Phys. Chem. A 103 (1999) 7958–7971.
[31] D. de Graaf, S. le Rol, H. Hintzen, L. le Gendre, G. de With, Mixed oxidation states of Yb and Sm in Si–Al–O–N glasses, J. Eur. Ceram. Soc. 26 (2006) 2497–2501.
[32] P. Kempgens, R.K. Harris, Z. Yu, D.P. Thompson, Structural characterization of Li α-sialon ceramics by high-resolution Al and Si NMR spectroscopy, J. Mater. Chem. 11 (2001) 2507–2512.
[33] D. Massiot, Sensitivity and lineshape improvements of MQ-MAS by rotor-synchronized data acquisition, J. Magn. Reson. Ser. A 122 (1996) 240–244.